



# Effects of nanoparticles deposition on thermal behaviour of boiling nanofluids

Hooman Azimi<sup>1</sup> · Zahra Baniamerian<sup>1</sup>

Received: 3 April 2017 / Accepted: 5 April 2018 / Published online: 22 May 2018  
© Springer-Verlag GmbH Germany, part of Springer Nature 2018

## Abstract

Recently, nanofluids are employed as the new generation of coolants specifically in boiling-mode cooling systems. In the present study, the convection heat transfer of boiling nanofluids through micro/minichannels is analytically investigated. Effects of nanoparticles deposition on heat transfer and fluid flow behavior of boiling nanofluids are comprehensively discussed. Nanoparticles deposition during flow boiling is found to cause different effects due to corresponding thermal conductivities. The proposed model validation was found to be in a good accordance with the results of previous studies.

## 1 Introduction

Nowadays, flow boiling is used in a variety of industrial sectors, such as air conditioning, refrigeration, chemical engineering, aircraft environmental control, spacecraft, thermal management, high-power electronics component cooling, and nuclear reactor cooling [1, 2]. Conventional coolants in the heat transfer applications are mostly deficient in thermal properties which restricts the system overall thermal performance. In the last two decades, using nanoparticles especially metal particles, to improving thermal properties of the fluids, has been developed in a wide range of industries (e.g., cooling of microchips, cancer therapeutics and nuclear reactors). These new types of fluids, known as nanofluids, are the suspensions of nanometer-sized solid particles, rods or tubes in conventional coolants.

Adding nanoparticles to the pure boiling flow can improve the thermal performance of the pure fluid [3–5]. although in some cases, the contrary issue has been observed [5–7]. Henderson et al. [6] experimentally studied on the SiO<sub>2</sub> and CuO-nanofluids in flow boiling. They found that using of SiO<sub>2</sub> nanoparticles in the R-134a as the base fluid, decreases the heat transfer coefficient down to 55% relative to the pure

fluid. It was observed that by using the CuO nanofluid, heat transfer coefficient enhances more than 100% compared to the base fluid.

An experimental study by sarafraz and hormozi [8], showed a degradation of heat transfer coefficient by an increase in the volume concentration of nanoparticles. Chehade et al. [5] experimentally evaluated effects of Ag nanoparticles on the convective boiling heat transfer in minichannels. They found that Ag nanofluid provides much more heat transfer rate in comparison of the pure fluid. They claimed that an enhancement up to 165% can be achieved by volume concentrations lower than 0.0005%.

Microscopy-based observations of pipe wall in flow boiling of nanofluids, revealed that nanoparticle deposition on the boiling surface commonly occurs and the surface modification due to the deposition of nanoparticles, has a major role by influencing the fluid thermal behavior [9–11]. One of the parameters which mostly affected by nanoparticles deposition, is the critical heat flux (CHF). Most of the studies in the field of nanoparticle deposition, are devoted to pool boiling modes, while the effects of coated surface as a porous structure on the thermal behavior of the boiling flow are still not known. Some other studies on convective boiling, have mostly ignored the deposition effects.

Few works have concerned CHF in flow boiling of nanofluids. Kim et al. [12] evaluated CHF of Al<sub>2</sub>O<sub>3</sub> nanofluids experimentally. They found 70% enhancement in the CHF using Al<sub>2</sub>O<sub>3</sub> nanofluid for flow boiling. The enhancement was attributed to the deposition of the nanoparticles which result in the better wettability. Lee et al. [13]

✉ Zahra Baniamerian  
amerian@tafreshu.ac.ir

<sup>1</sup> Department of Mechanical Engineering, Tafresh University, Tafresh, Iran

experimentally observed 100% enhancement in the CHF of GO/water nanofluid in the subcooled flow boiling. It was found that the nanoparticles deposited on the surface, modifies the surface wettability by reducing the contact angle.

As stated before, most of available studies concerning thermal behavior of nanofluids in boiling mode are experimental; although there are few numerical studies in the literature, covering a few number of problems [14, 15]. Abedini et al. [14] proposed a numerical model using Mixture method for simulation of subcooled boiling of Al<sub>2</sub>O<sub>3</sub>/water nanofluids. Their results showed that thermal conductivity is the key factor responsible for nanofluid heat transfer enhancement. Due to the small number of numerical studies on the flow boiling of nanofluids [16–18] some studies on pure fluid flow boiling have also been investigated in the present study.

Baniamerian et al. [16] simulated the annular flow regime analytically. The purpose of the model was to predict the occurrence of the film dryout for different type of coolants. Harirchian et al. [17] conducted a numerical study to obtain heat transfer coefficient and pressure drop in slug flow and annular/wispy annular pure flow.

Using nanofluids as coolants in the boiling cooling systems are well accepted as the matter of CHF, HTC and dryout length increments. Since some thermal deterioration was reported in the literature, further studies must be accomplished to clarify the mentioned problem. Some parameters like Latent Heat of Evaporation (LHE), conductivity, surface conditions and etc. are changed because of using nanofluids instead of the pure fluid. The first two parameters were previously considered by [19, 20]. while the investigation of the other ones, is the main purpose of this study.

In the present study, effects of nanoparticles deposition on the thermal performance of the cooling system is investigated by a mathematical model. Effects of adding nanoparticles, and their types (with different thermal conductivities) and concentrations on heat transfer are comprehensively discussed. Different thicknesses of the deposition layer may affect the convective boiling of the fluid flow which has been comprehensively discussed for the annular flow regime in this study.

## 2 Model development

Annular regime of nanofluid in microchannels is investigated in this study. The geometry of the problem is shown in Fig. 1. The temperature-constant thermal boundary condition is assumed on the microchannel wall. The fluid flow is considered to be in annular regime at the inlet of the micro channel. Flow conditions at the inlet are set based on the onset of annular pattern. In the annular pattern, vapor flows at the center of the microchannel surrounded by liquid (nanofluid) as a thin film adjacent to the channel wall (Fig. 1). The liquid film is the

nanofluid which is modeled as a homogeneous mixture of the base fluid and nanoparticles. Due to entrainment contribution of mass transfer some liquid droplets are entrained in to the vapor flow and in this regard the vapor core is simulated as a homogenous mixture of the vapor and entrained droplets. The annular flow pattern provides the maximum amount of heat transfer among other flow patterns [21] This issue along with the fact that annular flow pattern is the last and the most stable experienced regime in two-phase flows, has augmented the prominence of this flow pattern more than a common regime of two-phase flow. The following assumptions are considered in the present study:

1. The annular flow is steady and incompressible.
2. Fluid is in saturation condition
3. The inlet working fluid is at saturation conditions and phases are at thermodynamic equilibrium.
4. Pressure is not uniform across the channel's cross-sectional area.
5. Gravity force is concerned.
6. Liquid film thickness is circumferentially uniform due to the strong surface tension effects in mini/micro-channels.
7. Three mechanisms of mass transfer including evaporation, entrainment and deposition are considered.
8. Mass transfer occurs only at the vapor–liquid interface.
9. The two phases, flow separately in the channel.
10. Effects of deposition of nanoparticles on the boiling surface are considered.

### 2.1 Nanofluids

Thermo-physical properties of nanofluids can be calculated by considering the nanofluid as a homogeneous mixture of the fluid and nanoparticles. In this regard, density of nanofluids,  $\rho_{inf}$  is correlated by Pak and Chu [22]:

$$\rho_{inf} = \rho_p \varnothing + \rho_f (1 - \varnothing) \quad (1)$$

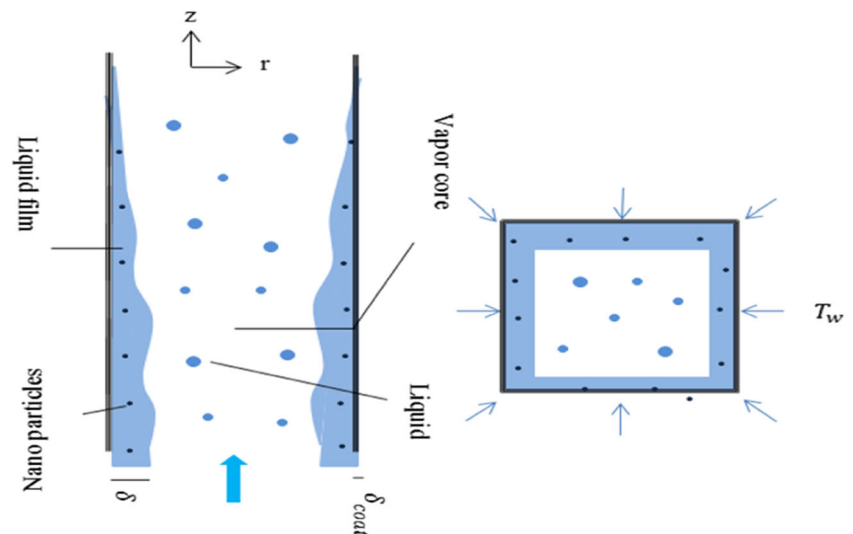
Where  $\rho_p$  and  $\varnothing$ , denotes particles density and particles volume fractions respectively. Also index “f” denotes the base fluid.

Dynamic viscosity of nanofluids  $\mu_{inf}$  can be computed by the following correlation [22]:

$$\mu_{inf} = \mu_f \left( \frac{1 + 0.5\varnothing}{(1 - \varnothing)^2} \right) \quad (2)$$

Nanoparticles' high conductivity, nanolayers ordering and the Brownian motions of nanoparticles are responsible for the higher conductivity of nanofluids [23]. Although some studies

**Fig. 1** Schematic of the investigated problem



indicate that the Brownian motions are not as effective as the other parameters on the conductivity of nanofluids [24–26]. The following equation is employed in this study for calculation of nanofluids conductivity [27]:

$$k_{inf} = ((k_p - k_{lr})\varnothing k_{lr} [2\gamma_1^3 - \gamma^3 + 1] + (k_p + 2k_{lr}) \times \gamma_1^3 [\varnothing\gamma^3 (k_{lr} - k_f) + k_f]) (\gamma_1^3 (k_p + 2k_{lr}) - (k_p - k_{lr})\varnothing [\gamma_1^3 + \gamma^3 - 1])^{-1} \quad (3)$$

In the above model, the solid/liquid interface around the nanoparticles, is considered individually as an effective layer on the conductivity.  $k_{lr}$  accounts for the thermal conductivity of the interfacial layer. As found by Zhao et al. [23],  $k_{lr}$  should not exceed the conductivity of the base fluid in solid phase. The conductivity of the pure water, which has been considered in this study, is about  $4k_f$  in solid phase. Thereupon thermal conductivity of nanolayers should lay in this range:

$$k_f < k_{lr} < 4k_f \quad (4)$$

So  $k_{lr}$  is assumed to be 3.75 times bigger than the thermal conductivity of the base fluid.  $\gamma$  and  $\gamma_1$  in Eq. (3) are defined by:

$$\gamma = 1 + \frac{h}{r_p} \quad \gamma_1 = 1 + \frac{h}{2r_p} \quad (5)$$

Thermal capacity of nanofluid is calculated by the correlation of Pak and Chu [22]:

$$cp_{inf} = \frac{(\varnothing\rho_p cp_p + (1-\varnothing)\rho_f cp_f)}{\rho_{inf}} \quad (6)$$

Where  $cp_p$  and  $cp_f$  are specific thermal capacities of nanoparticles and the base fluid respectively.

### 2.1.1 Effects of nanoparticles deposition

Deposition of nanoparticles on the channel wall especially when the evaporation enhances, results in a thin nanoparticle porous coating layer appearing on the solid surface during the evaporation process as shown in Fig. 2. This issue influences the fluid flow and thermal behavior of nanofluids. Consequently, a layer of nanoparticles deposition is considered on the walls along the channel.

The fluid flow through the porous coating layer can be characterized by the one-dimensional Darcy equation [28]:

$$\frac{dp_l}{dz} = \frac{\mu_f u_{coat}}{K_P} \quad (7)$$

Where  $u_{coat}$  accounts for the average fluid flow velocity through the porous coating layer and  $K_P$  denotes the permeability of the layer.

The liquid pressure gradient in both the liquid film and the porous coating layer is due to the liquid evaporation at the liquid–vapor interface not because of the extra force from the intrinsic meniscus [23]. Therefore, the liquid pressure gradient in the porous coating layer cannot be larger than that in the evaporating liquid film [23]. In this regard the maximum liquid pressure gradient in the porous coating layer is assumed to determine the pressure gradient in the liquid film.

Rearranging the Eq. (7) based on  $u_{coat}$ , gives:

$$u_{coat} = \frac{dp_l K_P}{dz \mu_f} \quad (8)$$

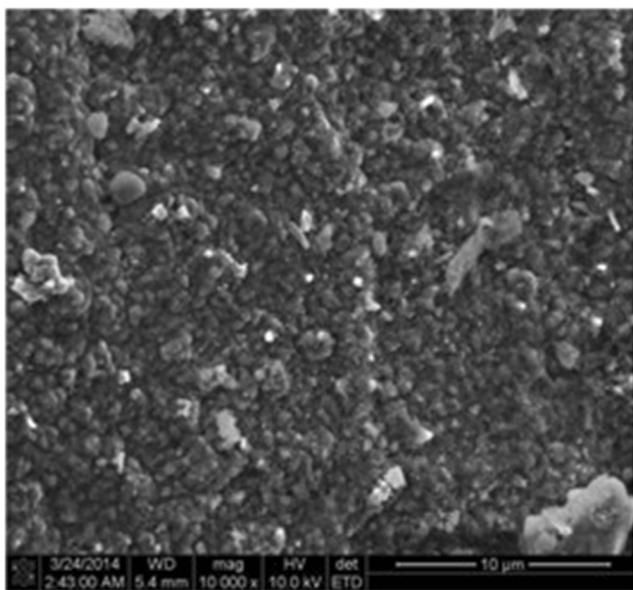


Fig. 2 SEM images of Al<sub>2</sub>O<sub>3</sub> nanoparticle-coated surface [26]

The permeability of the coating layer is calculated by using hydraulic radius model [29], assuming spherical shapes for nanoparticles:

$$K_P = \frac{\varepsilon^3}{36k_k(1-\varepsilon)^2} d_p^2 \tag{9}$$

$k_k$  is the Kozeny constant which is assumed 5 in this study [29].

## 2.2 Governing equations

### 2.2.1 Mass conservation

The total mass flow rate through the pipe,  $\dot{m}$  is consisted of liquid mass flow rate,  $\dot{m}_l$ , entrained mass of droplets,  $\dot{m}_e$  and vapor mass flow rate,  $\dot{m}_g$  which can be stated mathematically:

$$\dot{m} = \dot{m}_l + \dot{m}_g + \dot{m}_e \tag{10}$$

The ratio of each contribution to the total mass flow rate is specified as liquid film quality,  $l$ , entrained droplet quality,  $e$ , and vapor quality,  $x$ .

$$l = \frac{\dot{m}_l}{\dot{m}} \tag{11}$$

$$x = \frac{\dot{m}_g}{\dot{m}} \tag{12}$$

$$e = \frac{\dot{m}_e}{\dot{m}} \tag{13}$$

The vapor quality is set equal to the thermodynamic equilibrium quality.

By definite qualities for the vapor and entrained droplets at the onset of annular flow regime, liquid and vapor mass flow rates can be obtained:

$$\dot{m}_l = (1-x_0-e_0)\dot{m} \tag{14}$$

$$\dot{m}_g = x_0\dot{m} \tag{15}$$

$$\dot{m}_e = e_0\dot{m} \tag{16}$$

The initial vapor quality at the onset of annular flow regime is calculated from the proposed correlation of Taitel and Dukler [30]. In the model of Taitel and Dukler, the Martinelli parameter, with the definition as shown in Eq. 17, is assumed 1.6.

$$X_{vv} = \left( \frac{u_{lnf}}{u_g} \frac{1-x_0}{x_0} \frac{\rho_g}{\rho_{lnf}} \right)^{0.5} \tag{17}$$

$e_0$ , is the quality of entrained droplets at the onset of annular flow regime [31]:

$$e_0 = 0.951 - 0.32Ca^{0.21} \left( \frac{P}{P_{crnf}} \right)^{-0.42} \tag{18}$$

Where,  $P_{crnf}$  accounts for the critical pressure of the nanofluid. Capillary number,  $Ca$  is defined as:

$$Ca = \frac{u_{lnf}G}{\rho_{lnf}\sigma} \tag{19}$$

Mass conservation equation in integral form for the liquid film of the steady-state annular flow is in the following form:

$$\int \rho_{lnf} u_{lnf} dA + \frac{d \int \rho_{lnf} u_{lnf} dA}{dz} \Delta z - \int \rho_{lnf} u_{lnf} dA = \int \left[ (\Gamma_d - \Gamma_{en}) \Delta z \right] ds_i + \int \Gamma_{ev} \Delta z ds_h \tag{20}$$

The following conservation of mass can be written for the vapor phase flowing at the core:

$$\int \rho_g u_g dA + \frac{d \int \rho_g u_g dA}{dz} \Delta z - \int \rho_g u_g dA = \int \Gamma_{ev} \Delta z ds_h \tag{21}$$

Liquid film mass flow rate, vapor flow rate and the mass flow rate of entrained droplets are written as:

$$\dot{m}_l = \int \rho_{lnf} u_{lnf} dA \tag{22}$$

$$\dot{m}_g = \int \rho_g u_g dA \quad (23)$$

By applying the latter two equations in the integral forms of mass conservation, and some algebraic simplifications, the integral form of mass conservations will be:

$$\frac{d\dot{m}_l}{dz} = (\Gamma_d - \Gamma_{en})P_{co} - \Gamma_{ev}P_h \quad (24)$$

$$\frac{d\dot{m}_g}{dz} = (\Gamma_{ev})P_h \quad (25)$$

Also for the entrained droplets the mass conservation is written as:

$$\frac{d\dot{m}_e}{dz} = (\Gamma_{en} - \Gamma_d)P_{co} \quad (26)$$

$P_h$  and  $P_{co}$  are the microchannel and the vapor core perimeters respectively:

$$P_h = 4D \quad (27)$$

$$P_{co} = 4(D - 2\delta) \quad (28)$$

$\Gamma_{ev}$  is the evaporative flux of mass transfer:

$$\Gamma_{ev} = \frac{q''}{h_{fg}} \quad (29)$$

Heat flux is then can be calculated by the Newton cooling law:

$$q'' = h(T_w - T_i) \quad (30)$$

Where  $h$ , denotes the convective heat transfer coefficient and the dominant mechanism of deposited layer and liquid film is the conduction heat transfer. Consequently,  $h$  is obtained by use of Eq. (31):

$$h = \left[ \left( \frac{\delta_{coat}}{k_{coat}} + \frac{\delta}{k_{inf}} \right) \right]^{-1} \quad (31)$$

$\delta_{coat}$  is the thickness of the nanoparticle deposition layer that assumed to be uniformly formed on the inner surface of the channel. In the present modeling, thickness of the deposition layer is assumed to be between 0 to 10  $\mu\text{m}$  based on the experimental results [32–34].  $k_{coat}$  in the above relation accounts for the thermal conductivity of the porous layer which is obtained by [29]:

$$k_{coat} = \left[ 4^* \ln \left( \frac{k_p}{k_f} \right) - 11 \right] k_f \quad (32)$$

$T_w$ , is the wall temperature and  $T_i$  is the temperature of the interface between liquid film and the vapor core which is calculated using Clausius-Clapeyron relation:

$$T_i = T_g \left( 1 + \frac{\Delta P_i}{\rho_g h_{fg} - \frac{\Delta P_i}{2}} \right) \quad (33)$$

Where  $\Delta P_i$  stands for the saturation pressure difference at the interface (Eq. 34) and  $T_g$  is the saturation temperature at the saturation conditions.

$$\Delta P_i = p_g - p_l \quad (34)$$

$\Gamma_d$ , is the deposition contribution of mass transfer [35]:

$$\Gamma_d = kC \quad (35)$$

$$C = \frac{\dot{m}_e}{m_g/\rho_g + m_e/\rho_{inf}} \quad (36)$$

$k$ , the deposition factor which is obtained by [29]:

$$k = 0.0018 u_{co} \left( \frac{\rho_g u_{co} D}{\mu_g} \right)^{-0.26} \left( \frac{C}{\rho_g} \right)^{-0.28} \left( \frac{\rho_g}{\rho_{inf}} \right)^{0.63} \left( \frac{P_g}{P_{crmf}} \right)^{-1.57} \quad (37)$$

The properties related to the vapor core, shown with the index “co”, by the assumption of homogeneous mixture can be written in the following forms:

$$u_{co} = \frac{\dot{m}_g + \dot{m}_e}{\rho_{co} A_{co}} \quad (38)$$

$$\rho_{co} = \frac{1}{x_{co}/\rho_g + (1-x_{co})/\rho_{inf}} \quad (39)$$

$$A_{co} = (D - 2\delta)^2 \quad (40)$$

In the present study it is assumed that the entrainment takes place as the result of two possible events; first,  $\Gamma_{en1}$ , sweeping a fraction of wave crest off into the vapor core [36] and second breaking the vapor bubbles at the liquid-vapor interface. The first mechanism for transferring liquid droplets into the vapor core is correlated as [37]:

$$\Gamma_{en1} = 1.175 \times 10^{-4} u_g \mu_{inf} (Re_l - Re_g) \sqrt{\frac{\rho_{inf}}{\rho_g}} \quad \text{if } Re_l > Re_\infty \quad (41)$$

Where  $Re_\infty$ , known as the critical Re number is defined by [37]:

$$Re_\infty = \exp \left( 5.8504 + 0.4249 \left( \frac{\mu_g}{\mu_{inf}} \right) \right) \sqrt{\frac{\rho_{inf}}{\rho_g}} \quad (42)$$

$\Gamma_{en2}$ , the contribution of entrainment due to the bubbles breaking at the interface is correlated by [38]:

$$\Gamma_{en2} = 663 \left( \frac{q''}{h_{fg}} \right)^{2.5} \left( \frac{\delta}{\sigma \rho_g} \right)^{0.75} \quad (43)$$

Total magnitude of entrainment can be written as:

$$\Gamma_{en} = \Gamma_{en1} + \Gamma_{en2} \tag{44}$$

### 2.2.2 Momentum conservation

Momentum conservation in the vapor core is the balance between the pressure forces and two types of momentum forces, one due to the vapor flow and the other due to the mass transfers. The conservation of momentum in integral form, for a control volume of length  $\Delta z$  and the cross section which is equal to the vapor core, as shown in Fig. 3 is written as:

$$\begin{aligned} & \int P_g dA_{co} - \left( \int P_g dA_{co} + \frac{d(\int P_g A_{co})}{dz} \Delta z \right) \\ & - \int \tau_i \Delta z ds_i - \int \rho_{co} g dv_{co} \\ & = \left( \int \rho_{co} u_{co}^2 dA_{co} + \frac{d(\int \rho_{co} u_{co}^2 dA_{co})}{dz} \Delta z \right) - \int \rho_{co} u_{co}^2 dA_{co} \\ & + \int [\Gamma_d u_{co} \Delta z - \Gamma_{en} u_i \Delta z] ds_i - \int \Gamma_{ev} u_i \Delta z ds_h \end{aligned} \tag{45}$$

$\tau_i$  and  $u_i$  in Eq. (45) accounts for interfacial stress and interfacial velocity respectively.

Neglecting variations in perpendicular direction respect to the flow, in the liquid film as well as momentum change due to acceleration, the momentum conservation equation is simplified in the following form:

$$\begin{aligned} & \left[ -\frac{d(P_g A_{co})}{dz} \Delta z \right] - \tau_i P_{co} \Delta z - \rho_{co} g A_{co} \Delta z \\ & = + \frac{\rho_{co} u_{co}^2 d(A_{co})}{dz} \Delta z + [\Gamma_d u_{co} \Delta z - \Gamma_{en} u_i \Delta z] \\ & \quad P_{co} - \Gamma_{ev} u_i \Delta z P_h \end{aligned} \tag{46}$$

The core cross section varies in the flow direction due to the mass transfers mechanisms:

$$\frac{d(A_{co})}{dz} = -4(D-2\delta) \frac{d\delta}{dz} \tag{47}$$

At last, by employing Eq. (47), the integral form of momentum conservation for the vapor core will be:

$$\begin{aligned} -A_{co} \frac{d(P_g)}{dz} & = [-P_g P_{co} - \rho_{co} u_{co}^2 P_{co}] \frac{d\delta}{dz} \\ & + [\Gamma_d u_{co} - \Gamma_{en} u_i + \tau_i] P_{co} - \Gamma_{ev} u_i P_h + \rho_{co} g A_{co} \end{aligned} \tag{48}$$

Vapor core pressure gradient is obtained from Eq. (49):

$$\frac{d(P_g)}{dz} = - \frac{[-P_g P_{co} - \rho_{co} u_{co}^2 P_{co}] \frac{d\delta}{dz}}{\frac{A_{co}}{[\Gamma_d u_{co} - \Gamma_{en} u_i + \tau_i] P_{co} - \Gamma_{ev} u_i P_h} - \rho_{co} g}} \tag{49}$$

The interfacial shear stress is the result of velocity differences between the vapor core and interface and it can be calculated by the correlation:

$$\tau_i = \frac{1}{2} f_i \rho_{co} (u_{co} - u_i)^2 \tag{50}$$

Where,  $f_i$  is the interfacial friction factor. Interfacial friction factor  $f_i$  can be obtained by applying the empirical correlation of Shah and London [39]:

$$\begin{aligned} f_i & = \frac{16}{Rec} \text{ for } Rec < 2000 \\ f_i & = 0.079 Rec^{-0.25} \text{ for } 2000 < Rec < 20000 \\ f_i & = 0.046 Rec^{-0.2} \text{ for } Rec > 20000 \end{aligned} \tag{51}$$

Where, the effective Re Number,  $Rec$  is defined as:

$$Rec = \frac{\rho_{co} (u_{co} - u_i) D}{\mu_g} \tag{52}$$

The interfacial velocity is assumed  $u_i = 0.25 u_g$ .

For the liquid control volume shown in Fig. 4, ignoring inertial terms, the momentum balance will be:

$$\begin{aligned} & \int P_l dA_f - \left( \int P_l dA_f + \frac{d(\int P_l A_f)}{dz} \Delta z \right) + \int \tau_i \Delta z ds_i \\ & - \int \tau_f \Delta z ds_f - \int \rho_{lf} g v_f \\ & = \int [-\Gamma_d u_{co} \Delta z + \Gamma_{en} u_i \Delta z] ds_i + \int \Gamma_{ev} u_i \Delta z ds_h \end{aligned} \tag{53}$$

The cross section of the considered control volume of length  $\Delta z$  is:

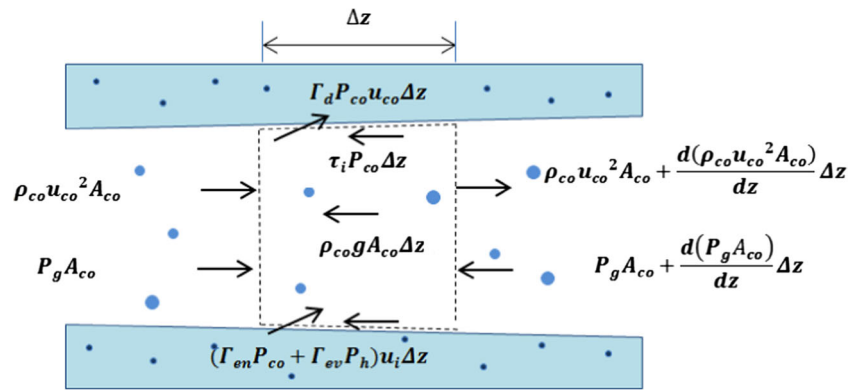
$$A_f = 4(r_f^2 - r_i^2) \tag{54}$$

Where,  $r_i$  is the distance between the pipe axis and the interface in perpendicular direction respect to the flow.  $r_f$  denotes the distance between the pipe axis and the upper face of the liquid element.

The momentum conservation in a more simplified form is:

$$\begin{aligned} -\frac{A_f dP_l}{dz} \Delta z + \tau_i P_{co} \Delta z - \tau_f P_f \Delta z - \rho_{lf} g A_f \Delta z \\ = [-\Gamma_d u_{co} \Delta z + \Gamma_{en} u_i \Delta z] P_{co} + \Gamma_{ev} u_i \Delta z P_h \end{aligned} \tag{55}$$

**Fig. 3** Momentum balance in the vapor core



$P_f$  is the control volume perimeter:

$$P_f = 8r_f \tag{56}$$

Reordering the above equations to obtain liquid film shear stress:

$$\tau_f = \left[ \frac{-\left(\frac{dP_l}{dz} + \rho_{lnf}g\right)(r^2 - r_i^2)}{2r} + \frac{[\tau_i + \Gamma_d u_{co} - \Gamma_{en} u_i] 2r_i - \Gamma_{ev} u_i D}{2r} \right] \tag{57}$$

Substituting the left hand side of Eq. (57) by the principle definition of the shear stress,  $\tau_f = \mu_{lnf} \frac{du_l}{dr}$ , and integrating the obtained equations, the liquid film velocity is achieved:

$$u_l = \frac{1}{\mu_{lnf}} \int \left[ \frac{-\left(\frac{dP_l}{dz} + \rho_{lnf}g\right)(r^2 - r_i^2)}{2r} + \frac{[\tau_i + \Gamma_d u_{co} - \Gamma_{en} u_i] 2r_i - \frac{\Gamma_{ev} u_i D}{2r}}{2r} \right] dr \tag{58}$$

$$u_l = \frac{1}{\mu_{lnf}} \left[ -0.5 \times \left( \frac{dP_l}{dz} + \rho_{lnf}g \right) \left( \frac{r^2}{2} - r_i^2 \ln r \right) + \left[ \tau_i + \Gamma_d u_{co} - \Gamma_{en} u_i \right] r_i \ln r - \Gamma_{ev} u_i r_w \ln r + C_l \right] \tag{59}$$

The velocity at the liquid interface is assumed:

$$u_w = u_{coat} \tag{60}$$

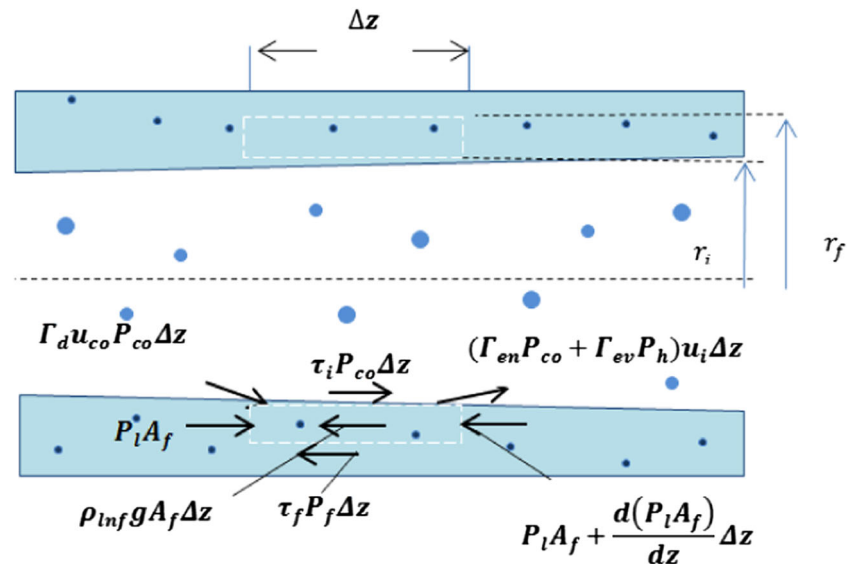
Liquid mass flow rate, by the principle definition of

$\dot{m}_l = \int_{r_i}^{r_w} \rho_l u_l dA$ , ( $dA = P_{co} dr$  can be calculated as:

$$\dot{m}_l = \frac{P_{co} \rho_{lnf}}{\mu_{lnf}} \left[ -0.5 \times \left( \frac{dP_l}{dz} + \rho_{lnf}g \right) \left( \frac{r^3}{6} - r_i^2 (r \ln r - r) \right) + \tau_i r_i (r \ln r - r) + \left[ \Gamma_d u_{co} - (\Gamma_{en} + \Gamma_{ev} r_w / r_i) u_i \right] r_i (r \ln r - r) + C_l r \right]_{r_i}^{r_w} \tag{61}$$

Liquid film pressure gradient is calculated using modified form of Young-Laplace equation [16]:

**Fig. 4** Momentum balance in the liquid film



$$P_l = P_g - (\Gamma_{ev}v_g + \Gamma_{en}v_l) - \frac{\sigma}{r_i} \quad (62)$$

Where  $r_i$  is hydraulic radius of the channel,  $v_l$  and  $v_g$  are radial velocities of liquid film and vapor core at the interface.

$$v_g = \frac{\Gamma_{ev}}{\rho_g} \quad (63)$$

$$v_l = \frac{\Gamma_{en}}{\rho_{lnf}} \quad (64)$$

### 3 Solution procedure

The mass flow conditions are known, at the pipe inlet. The pipe hydraulic diameter is 1.1 mm, pipe length is 0.62 m, and mass flow velocity is considered as 230–300 kg/m<sup>2</sup>.s. The pipe wall is supposed to be at constant temperature of 411.6 K. For the considered mass flow rate in the present modeling, temperature differences greater than 10 K and even around 10 K make the liquid film thickness vanish and therefore dryout happens. In this regard the difference between the pipe wall and the saturation temperature of the flow at the pipe inlet is assumed in the range of 2.5–10 K to avoid dryout along the channel.

The flow in stream-wise direction is meshed with several elements of length  $dz$  to accomplish the computation procedure:

1. First the thermophysical properties of nanofluids are calculated employing Eqs. (1, 2, 3, 6).
2.  $x_0$  and  $e_0$  values at the onset of annular flow regime are calculated by Eqs. (17, 18).
3. Individual contributions of initial mass flow rates are calculated by (14–16).
4. Assuming a value for the liquid film thickness,  $\delta$  of the next element, areas and perimeters of the element will be calculated.
5. Different contributions of mass transfer are calculated by Eqs. (29, 35 and 44)
6. Using Eqs. (24–26) mass flow rates of liquid film as well as vapor and entrained droplets are obtained.
7. Vapor core pressure gradient is computed by Eq. (49).
8. Liquid film pressure gradient is obtained through Eq. (62)
9. Liquid film mass flow rate is calculated by Eq. (61) and if the obtained magnitude is consistent with what achieved from Eq. (24) the solution is completed for this element; otherwise steps 4–9 are repeated.
10. Steps 4–10 are repeated for the other elements and the procedure will last until dryout occurs.
11. Heat transfer coefficient is then evaluated using Eq. (31).

A brief solution procedure is shown in Fig. 5.

### 4 Verification of the model

In order to validate the present model, the experimental data of Wang et al. [40] and Moreira et al. [41] are used. In the first validation, results of the present model have been compared with experimental results of Wang et al. [40]. In the Fig. 6, the Nusselt Number against wall heat flux for 0.1 vol.% aluminum oxide nanofluid have been plotted in the similar fluid flow and geometrical conditions. The average relative error is 4.56% (MAE of 0.9%) and maximum error is 7.01%. In the second validation, results of the present model have been plotted against the experimental data of Moreira et al. [41] (Fig. 7). Local heat transfer variations of 0.1 vol.% Cu nanofluid versus the vapor quality for the both works, as can be seen in Fig. 7, are in good agreement. An average relative error of 6.36% (MAE of 0.7%) and maximum error of 11.36% is observed between the results of present model and those of [41].

### 5 Results and discussion

There is a possibility of sedimentation of nanoparticles on the channel wall; this phenomenon may influence the performance of the convective boiling. Although for the very low

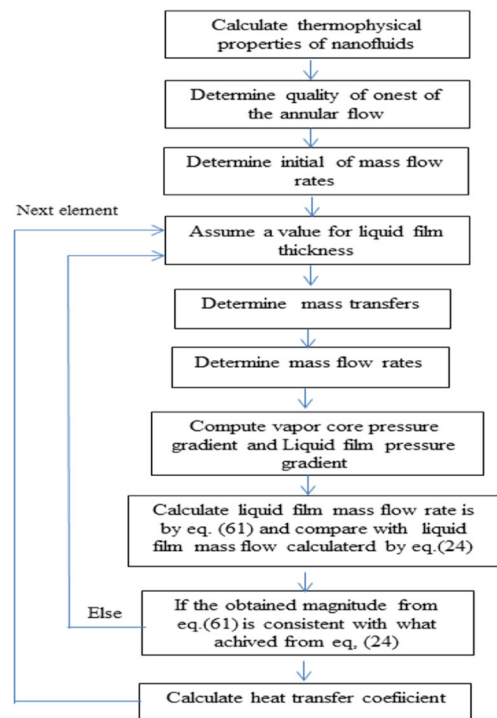
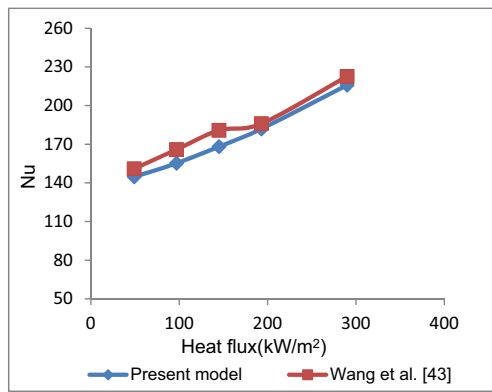


Fig. 5 Solution procedure





**Fig. 6** Variations of Nusselt Number for 0.1 vol% of  $\text{Al}_2\text{O}_3$  nanofluids against heat flux in comparison with results of [40]

nanoparticles concentrations, nanoparticles deposition on the surface in the base fluid can be ignored [42]. The deposited nanoparticles on the wall forms a thermal resistance, slows down the evaporation rate as well as the heat transfer. On the other hand, high conductivities of nanoparticles in nanofluid can enhance the evaporation rate and heat transfer. From the implementation above, it can be concluded that particle deposition and thermal conductivity act in reverse manners.

Variations of heat transfer coefficient against nanoparticles concentration is demonstrated in Fig. 8 for  $\text{TiO}_2$ , Ni and ZnO water based nanofluids. Particle deposition during the flow boiling is ignored. The higher conduction factor of nanoparticles, implies that the nanofluid is more conductive, the evaporation rate is higher and the thickness of the liquid film is thinner. Consequently, in a specific volume fraction, heat transfer coefficient will increase. Also increasing the volume concentration enhances the thermal conductivity of nanofluids and subsequently heat transfer coefficient will increase. The maximum amounts of enhancement in the heat transfer coefficient in comparison with the pure water for Ni, ZnO and  $\text{TiO}_2$  nanofluids are 52.2, 43.4 and 36.4% respectively.

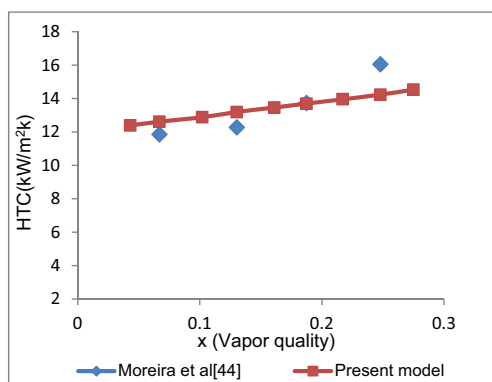


**Fig. 7** Variations of Heat transfer coefficient for 0.1 vol% of Cu nanofluids against vapor quality in comparison with results of [41]

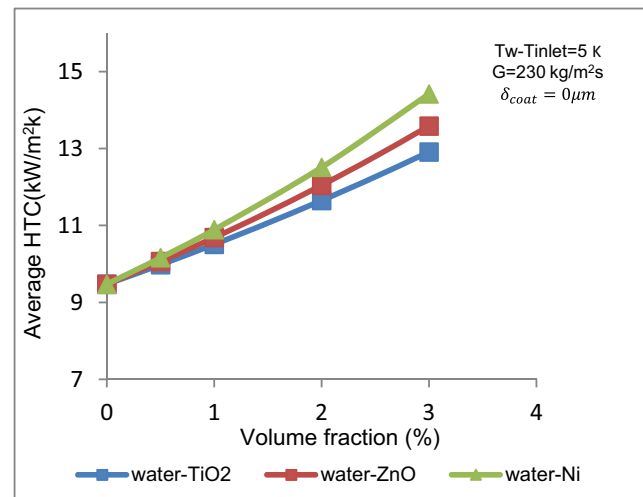


**Fig. 8** Average HTC against volume fraction of nanoparticles

Figure 8 is plotted again but in this figure the effects of particles deposition on the channel wall is considered (Fig. 9). Single deposited layer with  $5 \mu\text{m}$  thickness is supposed for Ni,  $\text{TiO}_2$  and ZnO nanofluids. As noted before HTC of nanofluids enhances as the nonparticle concentration are increased. Also for a specific thickness of the deposition layer, by increasing the thermal conductivity of nanoparticles, thermal conductivity of deposition layer will increase (based on Eq. 34). Which leads to a decrement in the deposition resistance. In this regard for the  $\text{TiO}_2$  nanofluid, HTC becomes lower compared to pure water owing to lower conductivities of  $\text{TiO}_2$ . It can be concluded that in the specified conditions, the deposition layer affects the HTC much more than the thermal conductivity. Although in high volume concentrations, the thermal conductivity may play pivotal role compared to the deposition layer.

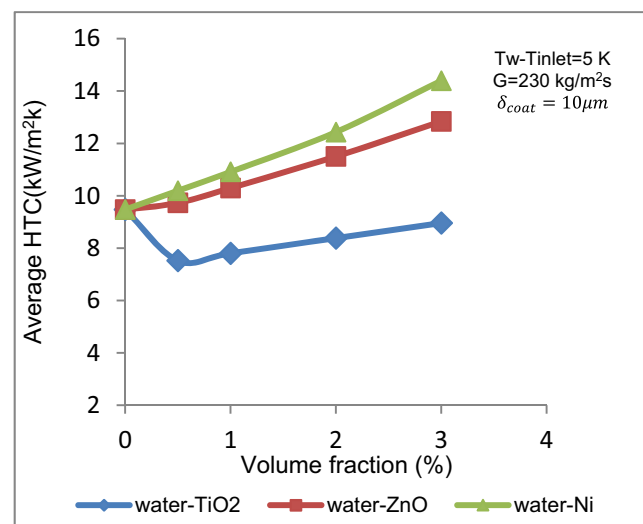


**Fig. 9** Variations of heat transfer coefficient against volume concentration

Thermal conductivity of ZnO nanoparticles is greater than that of  $\text{TiO}_2$  therefore thermal resistance is not as effective as the thermal conduction in the heat transfer. In this regard HTC of the ZnO nanofluid is more than the pure water. HTC for the Ni nanofluid is higher than the HTC of pure water and also higher than the HTC of the ZnO nanofluid due to the high thermal conductivities of Ni nanoparticles. For the considered range, the maximum enhancement in the HTC is 51.9% corresponding to 3 vol.% of Ni nanofluid while the maximum decrease in HTC is 20.5% corresponding to 0.5 vol% of  $\text{TiO}_2$  nanofluid. Heat transfer coefficient of  $\text{TiO}_2$  nanofluid versus volume concentration, for the variety of deposition layers, is demonstrated in Fig. 10. In case of the zero thickness of deposition layer, HTC increases compared to the pure water. By increasing the thickness of the deposition layer, thermal resistance will increase significantly and can reduce the HTC. Due to the inverse effects of conductivity and the deposition thickness, it may be possible to prevent HTC reduction by increasing the volume concentration of nanoparticles.

Similar curves are provided for the ZnO nanofluids in the Fig. 11. It can be found from the figure that effects of thermal resistance due to the deposition layer in decreasing HTC is fractional compared to the effects of nanoparticles conductivity in increasing the HTC. Thereupon, in the specified conditions the deposition layer cannot avoid the enhancement of the HTC by increasing volume concentration of nanoparticles.

Effects of deposition layer on the Ni nanofluid in the different volume fractions and for the variety of deposition layers investigated in Fig. 12. In the Ni nanofluid similar to the mentioned information about for the ZnO nanofluid, effects of thermal resistance due to the deposition layer in

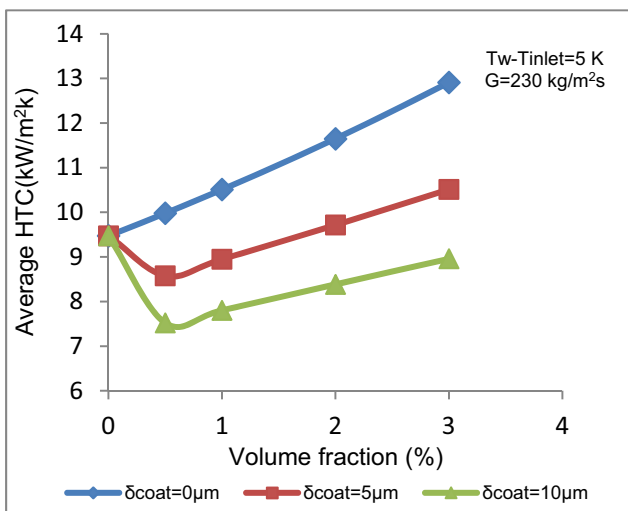


**Fig. 10** HTC of  $\text{TiO}_2$  nanofluid for different volume concentrations and deposition thicknesses

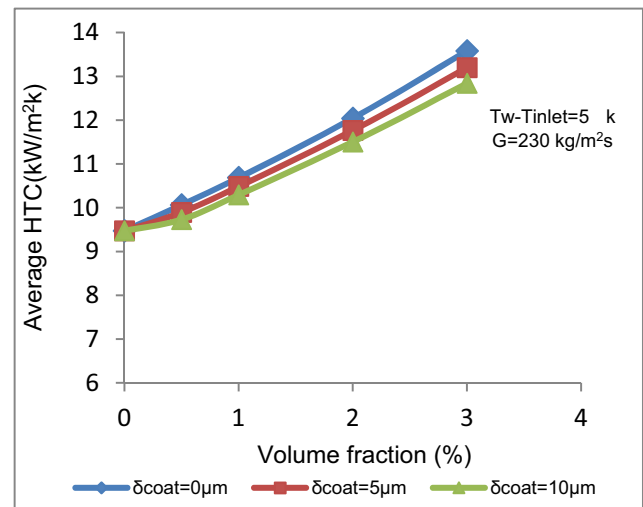


**Fig. 11** HTC of ZnO nanofluid for different volume concentrations and deposition thicknesses

decreasing HTC is negligible compared to the effects of nanoparticles conductivity in enhancement the HTC. Thereupon the deposition layer cannot avoid the increase in the HTC by increasing volume concentration of nanoparticles.

Figure 13 shows the local evaporative heat flux of 1 vol.%  $\text{TiO}_2$  nanofluid against the dimensionless length of the channel. As can be seen from the figure, the evaporative heat flux enhances along the channel due to the increase in temperature difference in between the channel wall and the saturation temperature (which is known as “temperature difference” here after) of the nanofluid. Also By increasing the temperature difference at the channel inlet, the evaporative heat flux and subsequently the evaporation rate intensifies.

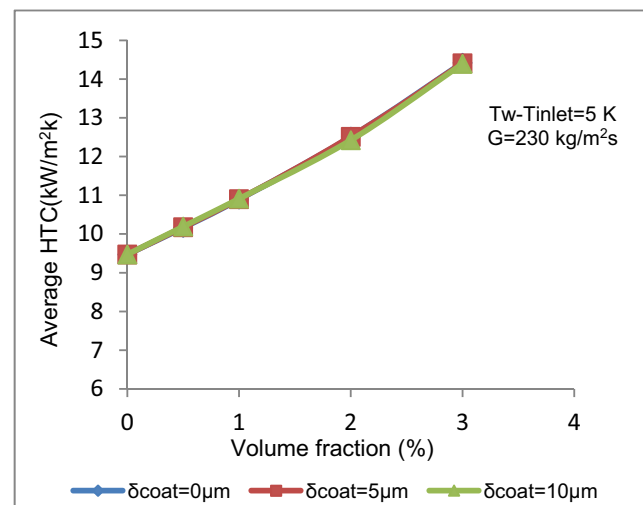


**Fig. 12** HTC of Ni nanofluid for different volume concentrations and deposition thicknesses

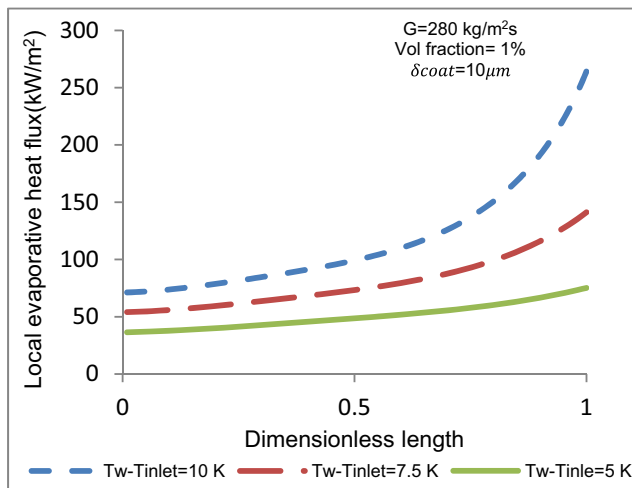


**Fig. 13** Local evaporative heat flux against the channel dimensionless length for  $\text{TiO}_2$  nanofluid

Variations of liquid film thickness along the channel is shown for 1 vol%  $\text{TiO}_2$  nanofluid in Fig. 14. The channel length is used to nondimensionalize the length scales. As can be observed in the figure the liquid film thins down along the channel. Increasing the temperature difference at the channel inlet accelerates the evaporation and enhances the liquid film reduction. Although the reduction in the thickness of the liquid film, in turn, increases the evaporation rate. In other words, liquid film thickness reduces due to the evaporation of nanofluid and the reduction in the liquid thickness, itself, intensifies the evaporation rate.

Heat transfer coefficient, in Fig. 15, is compared for the considered nanofluids against the temperature difference at the channel inlet. Increasing the temperature difference at the channel inlet, result in an enhancement in the evaporation rate, a decrease in the liquid film thickness and subsequently an enhancement of the HTC.

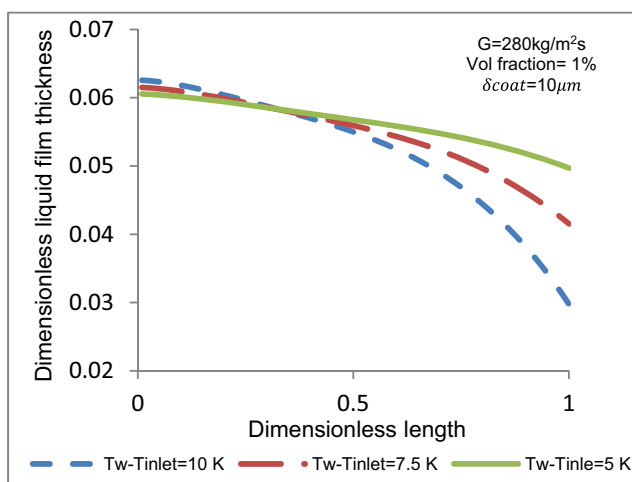


**Fig. 14** Variations of  $\text{TiO}_2$  nanofluid film thickness along the channel

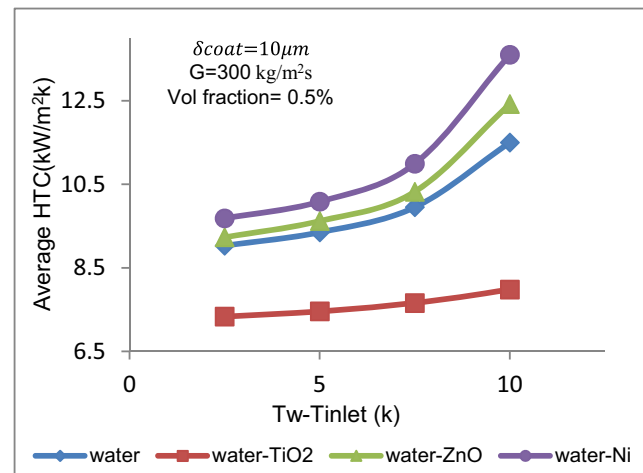


**Fig. 15** Variations of HTC against the inlet temperature difference

Pressure drop variations for variety of temperature differences are demonstrated in Fig. 16. As can be found from the figure, pressure drop enhances by increasing the temperature difference at the channel inlet. Increasing the temperature difference enhances the rate of vaporization which reduces the liquid film thickness and increases the vapor velocity. The latter intensifies the frictional and dynamic pressure drop and subsequently the total pressure drop. In this regard, at a specified temperature difference Ni nanofluid has the maximum pressure drop. In contrary,  $\text{TiO}_2$  nanofluid has the minimum pressure drop.

## 6 Conclusion

An analytical model for the heat and fluid flow of boiling nanofluids considering effects of nanoparticles deposition is

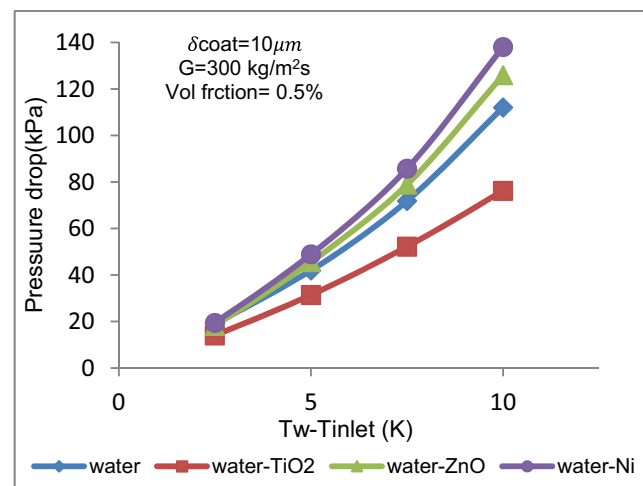


**Fig. 16** Pressure drop against the temperature difference at the channel inlet

proposed in the present study. Thermal and hydraulic behavior of three nanofluids ( $\text{TiO}_2$ ,  $\text{ZnO}$  and  $\text{Ni}$ ) are compared to the pure water. For the highly conductive nanoparticles, effect of thermal resistance, due to the nanoparticles deposition, on the thermal/hydraulic performance of the cooling system is found negligible as it cannot influence HTC and pressure drop significantly. Instead, for poorly conductive nanoparticles, deposition phenomenon plays an important role in thermal and hydraulic performance of the cooling system. Deposition in these kinds of system can influence the HTC much more than the thermal conductivity. In such situations the HTC becomes lower than that of pure water. The maximum enhancement in the HTC, considering effects of nanoparticles deposition, is 51.9% for the 3 vol.%  $\text{Ni}$  nanofluid and the maximum decrease of 20.5% is found for 0.5 vol.%  $\text{TiO}_2$  nanofluid. Although by increasing volume concentration of nanoparticles the effective thermal conductivity of the nanofluid can be enhanced so that even for poorly conductive nanoparticles, effects of deposition layer can be neutralized.

### Publisher's Note

Springer Nature remains neutral with regard to jurisdictional claims in published maps and institutional affiliations.

### References

- Fang X, Zhou Z, Li D (2013) Review of correlations of flow boiling heat transfer coefficients for carbon dioxide. *Int J Refrig* 36(8): 2017–2039
- Zhang H, Mudawar I, Hasan MM (2009) Application of flow boiling for thermal management of electronics in microgravity and reduced-gravity space systems. *IEEE Trans Compon Packag Technol* 32(2):466–477
- Peng H, Ding G, Jiang W, Hu H, Gao Y (2009) Heat transfer characteristics of refrigerant-based nanofluid flow boiling inside a horizontal smooth tube. *Int J Refrig* 32(6):1259–1270
- Lee S-W, Park S-D, Kang S-R, Kim S-M, Seo H, Lee D-W, Bang I-C (2012) Critical heat flux enhancement in flow boiling of  $\text{Al}_2\text{O}_3$  and  $\text{SiC}$  nanofluids under low pressure and low flow conditions. *Nucl Eng Technol* 44(4):429–436
- Cehade AA, Gualous HL, Le Masson S, Fardoun F, Besq A (2013) Boiling local heat transfer enhancement in minichannels using nanofluids. *Nanoscale Res Lett* 8(1):130
- Henderson K, Park Y-G, Liu L, Jacobi AM (2010) Flow-boiling heat transfer of  $\text{R-134a}$ -based nanofluids in a horizontal tube. *Int J Heat Mass Transf* 53(5):944–951
- Baqeri S, Akhavan-Behabadi M, Ghadimi B (2014) Experimental investigation of the forced convective boiling heat transfer of  $\text{R-600a}$ /oil/nanoparticle. *Int Commun Heat Mass Transfer* 55:71–76
- Sarafraz M, Hormozi F (2014) Scale formation and subcooled flow boiling heat transfer of  $\text{CuO}$ -water nanofluid inside the vertical annulus. *Exp Thermal Fluid Sci* 52:205–214
- Kim SJ, McKrell T, Buongiorno J, Hu L-w (2010) Subcooled flow boiling heat transfer of dilute alumina, zinc oxide, and diamond nanofluids at atmospheric pressure. *Nucl Eng Des* 240(5):1186–1194
- Rana K, Rajvanshi A, Agrawal G (2013) A visualization study of flow boiling heat transfer with nanofluids. *J Vis* 16(2):133–143
- Vafaei S, Wen D (2011) Flow boiling heat transfer of alumina nanofluids in single microchannels and the roles of nanoparticles. *J Nanopart Res* 13(3):1063–1073
- Kim TI, Jeong YH, Chang SH (2010) An experimental study on CHF enhancement in flow boiling using  $\text{Al}_2\text{O}_3$  nano-fluid. *Int J Heat Mass Transf* 53(5):1015–1022
- Lee SW, Kim KM, Bang IC (2013) Study on flow boiling critical heat flux enhancement of graphene oxide/water nanofluid. *Int J Heat Mass Transf* 65:348–356
- Abedini E, Behzadmehr A, Sarvari S, Mansouri S (2013) Numerical investigation of subcooled flow boiling of a nanofluid. *Int J Therm Sci* 64:232–239
- Valizadeh Z, Shams M (2016) Numerical investigation of water-based nanofluid subcooled flow boiling by three-phase Euler–Euler, Euler–Lagrange approach. *Heat Mass Transf* 52(8):1501–1514
- Baniamerian Z, Mehdipour R, Aghanajafi C (2012) Analytical simulation of annular two-phase flow considering the four involved mass transfers. *J Fluids Eng* 134(8):081301
- Deng H, Fernandino M, Dorao CA (2015) Modeling of annular-mist flow during mixtures boiling. *Appl Therm Eng* 91:463–470
- Qu W, Mudawar I (2003) Flow boiling heat transfer in two-phase micro-channel heat sinks—II. Annular two-phase flow model. *Int J Heat Mass Transf* 46(15):2773–2784
- Baniamerian Z, Mashayekhi M (2017) Experimental assessment of saturation behavior of boiling nanofluids: pressure and temperature. *J Thermophys Heat Transf* 31:732–738
- Baniamerian Z, Mashayekhi M (2017) Evaporative behavior of gold-based hybrid nanofluids. *J Thermophys Heat Transf*. <https://doi.org/10.2514/1.T5220>
- Kreith F, Boehm RF (1999) Heat and mass transfer mechanical engineering handbook. CRC Press LLC, Boca Raton
- Pak BC, Cho YI (1998) Hydrodynamic and heat transfer study of dispersed fluids with submicron metallic oxide particles. *Exp Heat Transfer Int J* 11(2):151–170
- Zhao J-J, Duan Y-Y, Wang X-D, Wang B-X (2011) Effect of nanofluids on thin film evaporation in microchannels. *J Nanopart Res* 13(10):5033
- Shima P, Philip J, Raj B (2009) Role of microconvection induced by Brownian motion of nanoparticles in the enhanced thermal conductivity of stable nanofluids. *Appl Phys Lett* 94(22):223101
- Jang SP, Choi SU (2007) Effects of various parameters on nanofluid thermal conductivity. *J Heat Transf* 129(5):617–623
- Nan C-W, Birringer R, Clarke DR, Gleiter H (1997) Effective thermal conductivity of particulate composites with interfacial thermal resistance. *J Appl Phys* 81(10):6692–6699
- Murshed S, Leong K, Yang C (2008) Investigations of thermal conductivity and viscosity of nanofluids. *Int J Therm Sci* 47(5): 560–568
- Darcy H (1856) *Les fontaines publiques de la ville de Dijon: exposition et application*. Victor Dalmont
- Kaviany M (2012) *Principles of heat transfer in porous media*. Springer Science & Business Media
- Taitel Y, Dukler A (1976) A model for predicting flow regime transitions in horizontal and near horizontal gas-liquid flow. *AIChE J* 22(1):47–55
- Kim S-M, Mudawar I (2014) Theoretical model for local heat transfer coefficient for annular flow boiling in circular mini/micro-channels. *Int J Heat Mass Transf* 73:731–742
- Kumar CS, Suresh S, Praveen A, Kumar MS, Gopi V (2016) Effect of surfactant addition on hydrophilicity of  $\text{ZnO-Al}_2\text{O}_3$  composite and enhancement of flow boiling heat transfer. *Exp Thermal Fluid Sci* 70:325–334
- Sarwar MS, Jeong YH, Chang SH (2007) Subcooled flow boiling CHF enhancement with porous surface coatings. *Int J Heat Mass Transf* 50(17):3649–3657

34. Stutz B, Morceli CHS, Da Silva MDF, Cioulachtjian S, Bonjour J (2011) Influence of nanoparticle surface coating on pool boiling. *Exp Thermal Fluid Sci* 35(7):1239–1249
35. Whalley P, Hutchinson P, Hewitt G (1973) The calculation of critical heat flux in forced convection boiling, vol 7520. AERE
36. Baniamerian Z, Aghanajafi C (2010) Simulation of entrainment mass transfer in annular two-phase flow using the physical concept. *J Mech* 26(3):385–392
37. Schadel S, Leman G, Binder J, Hanratty T (1990) Rates of atomization and deposition in vertical annular flow. *Int J Multiphase Flow* 16(3):363–374
38. Ueda T, Inoue M, Nagatome S (1981) Critical heat flux and droplet entrainment rate in boiling of falling liquid films. *Int J Heat Mass Transf* 24(7):1257–1266
39. Shah RK, London AL (2014) Laminar flow forced convection in ducts: a source book for compact heat exchanger analytical data. Academic
40. Wang Y, Deng K, Liu B, Wu J, Su G (2016) Experimental study on Al<sub>2</sub>O<sub>3</sub>/H<sub>2</sub>O nanofluid flow boiling heat transfer under different pressures. In: ASME 2016 5th International Conference on Micro/Nanoscale Heat and Mass Transfer. American Society of Mechanical Engineers, pp V001T002A002-V001T002A002
41. Moreira TA, do Nascimento FJ, Ribatski G, Group HTR (2017) An investigation of the effect of nanoparticle composition and dimension on the heat transfer coefficient during flow boiling of aqueous nanofluids in small diameter channels (1.1 mm). *Exp Thermal Fluid Sci* 89:72–89
42. Boudouh M, Gualous HL, De Labachellerie M (2010) Local convective boiling heat transfer and pressure drop of nanofluid in narrow rectangular channels. *Appl Therm Eng* 30(17):2619–2631